Journal of Computer-Aided Materials Design, **7:** 171–194, 2001.
KLUWER/ESCOM

Systems design of high performance stainless steels II. Prototype characterization

C.E. CAMPBELL* and G.B. OLSON
Department of Materials Science and Engineering,
Northwestern University, Evanston, IL 60208, U.S.A.
(Tel: 847-491-5222; Fax: 847-491-7820)

Received and accepted 2 April 2000

Abstract. Within the framework of a systems approach, the design of a high performance stainless steel integrated processing/structure/property/performance relations with mechanistic computational models. Using multicomponent thermodynamic and diffusion software platforms, the models were integrated to design a carburizable, secondary-hardening, martensitic stainless steel for advanced gear and bearing applications. Prototype evaluation confirmed the predicted martensitic transformation temperature and the desired carburizing and tempering responses, achieving a case hardness of R_c 64 in the secondary-hardened condition without case primary carbides. Comparison with a commercial carburizing stainless steel demonstrated the advantage of avoiding primary carbides to resist quench cracking associated with a martensitic start temperature gradient reversal. Based on anodic polarization measurements and salt-spray testing, the prototype composition exhibited superior corrosion resistance in comparison to the 440C stainless bearing steel, which has a significantly higher alloy Cr concentration.

Keywords: materials design, carburizing, anodic polarization, dilatometry, secondary-hardening, fracture-toughness

1. Introduction

A systems approach [1] to computational materials design was used to design a prototype high-performance stainless bearing steel. The first three steps of system design – establishment of the property objectives, the model development, and integration and optimization of the design models – were described in Part I [2]. Figure 1 illustrates the interconnections between the desired property objectives, structure, and processing for the design of a carburizing secondary-hardening, martensitic stainless steel. The next step of the systems design approach is the characterization of the design composition to determine whether the desired property objectives were obtained. Experimental evaluation of the design prototype also identifies the strengths and weaknesses of the design models applied. That is, if the prototype does not meet the required property objectives, then either the desired property objectives must be reevaluated or the design models must be improved.

This work describes the characterization of the prototype carburizing, secondary-hardening, martensitic stainless steel designed in Part I [2] and verifies whether the established property objectives were obtained. These objectives include a lath martensitic microstructure obtained with a M_s temperature greater than 150 °C, a carburized case that has a surface hardness exceeding R_c 62 and that does not include the formation of primary carbides, an aqueous corrosion resistance exceeding that of 440C, a rolling contact fatigue resistance equilvalent to

*Now at NIST, Metallurgy Division, 100 Bureau Dr. Stop 8555, Gaithersburg, MD, 20899-8555, U.S.A.

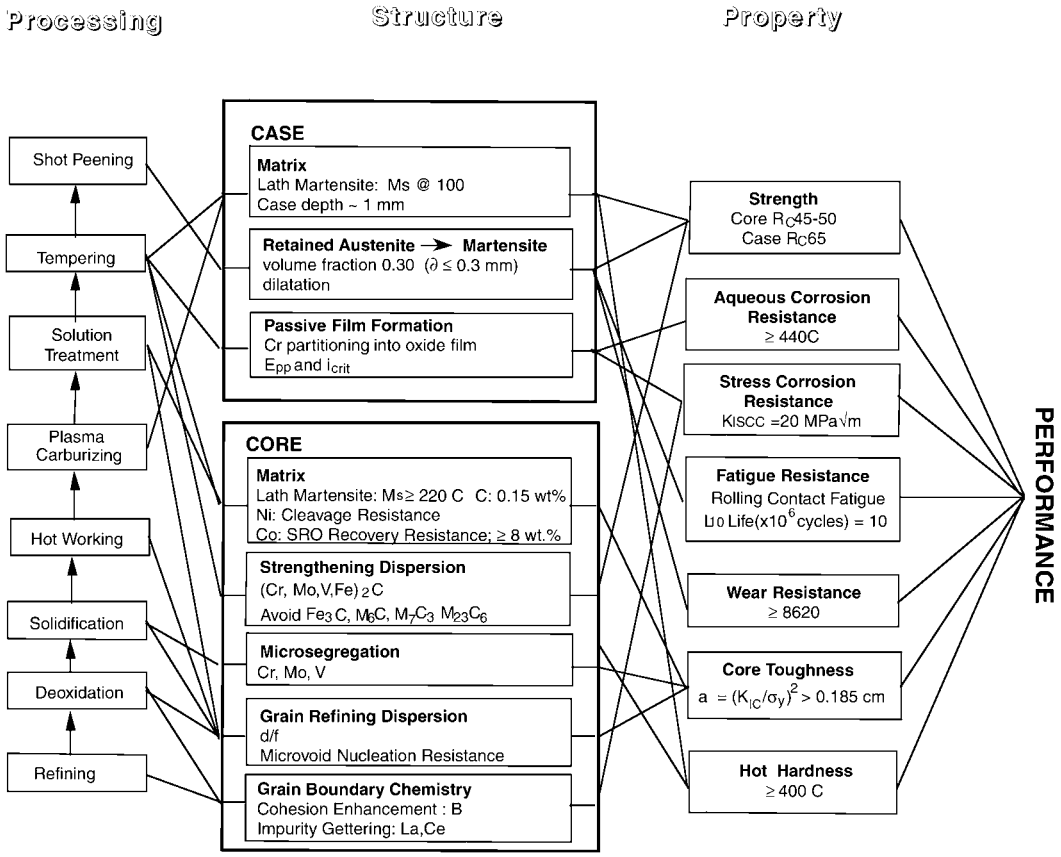

Figure 1. Flow block diagram of the processing/property/structure/performance interactions for a carburizing secondary-hardening stainless steel.

high temperature bearing alloys M50 and M50NiL, and a core toughness twice that of 440C. The characterization of this prototype includes comparisons to commercial stainless steels and various experimental alloys.

2. Materials and methods

2.1. Materials

An experimental, 22.68 kg (50 lb), vacuum induction melted heat of the design composition, CS62 [3], was produced by Republic Steel using standard Al and Ti deoxidation practices. Boron additions were made to improve grain boundary cohesion and cesium additions were made to getter sulfur and phosphorous impurities. After solidification, the ingot was reheated to 1232 °C (2250 °F) and forged to a 0.0584 m (2.3″) square bar. The forged bar was immediately reheated to 1232 °C and reduced to a 0.033 m (1.3″) square bar. The chemical analysis of the studied experimental heat of CS62 is given in Table 1. In general, the chemical analysis of the experimental composition corresponds to desired composition for the prototype. However,

Table 1. Alloy compositions (wt.%)

Element	Design Prototype (CS62)	AerMet100	AF1410	1605-8B	NASA1	Pyrowear 675
Fe	balance	balance	balance	balance	balance	balance
Co	15.51	13.10	14.25	15.8	22.53	5.4
Ni	1.56	11	10.5	4.88	8.48	2.6
Cr	9.13	3.0	2.1	7.87	11.75	13.0
Mo	0.002	1.18	1.05	1.5	0.3	1.8
V	0.21	NA	NA	NA	0.25	0.6
Si	<0.0002	0.04	NA	NA	0.01	0.4
Mn	0.02	0.01	NA	NA	<0.01	0.65
C	0.21 (core)	0.24	0.16	0.248	0.29	0.07 (core)
Al	0.008	0.001	0.005	–	–	–
B	0.0023	–	–	–	–	–
Ce	0.015	–	–	–	<0.001	–
La		–	–	–	<0.001	–
N	0.002	–	–	–	–	–
O	0.005	–	–	–	–	–
P	0.001	0.005	–	–	0.005	–
S	0.002	0.006	–	–	0.003	–
Ti	0.011	0.02	–	–	–	–

the oxide content at 0.005 wt.% O and the aluminum content at 0.008 wt.% are higher than expected in comparison to other commercial alloys. These compositions deviations may have an adverse effect on the material properties, especially the fracture toughness.

In characterizing the design alloy, the performance of the prototype was compared to two other alloys: the model secondary hardening steel 1605-8B [4] and the commercial carburizing martensitic stainless steel, Pyrowear 675 [5]. The 1605-8B alloy was produced by NKK Corporation using vacuum induction processing. Carpenter Technology provided rod material from an experimental heat of Pyrowear 675.

2.2. Experimental methods

Dilatometry was used to study the martensitic transformation using a computer controlled dilatometer. Cylindrical samples, 3 mm in diameter and 10 mm in length, were heated in an induction furnace and were quenched using helium gas. The temperature was monitored by a Pt-Pt10%Rh thermocouple spot welded directly to the sample surface. The dilatometry experiments were conducted under a vacuum of $<10^{-2}$ Pa. The thermal expansion and contraction were recorded as functions of temperature as the samples were heated at 500 °C/minute to a temperature above the austenitic finish temperature, A_f, then held at this temperature for 15 min, and finally quenched to room temperature. The austenitic and martensitic start (A_s, M_s) temperatures were identified by the discontinuous length changes.

Bulk and surface heat treatments were performed to produce the desired microstructures. The typical sample size for such treatments was a 0.0125 m cube. The solution treatments were performed with the material either encapsulated in quartz tubing or in an furnace back-filled with argon. Tempering to precipitate the strengthening dispersion was also performed in an inert environment. Using a hydrogen furnace, decarburizing experiments were conducted using polished samples of dimensions 2.5 mm $\times$ 5 mm $\times$ 20 mm.

Macro-hardness measurements were made using a Rockwell C tester on samples polished to a 600 grit finish. A Vickers indenter with a 100 g load was used to measure the micro-hardness on samples polished to a 1 μm finish.

Plane-strain fracture toughness testing was conducted following the ASTM standard E399 [6] for K_{IC} testing. The machined compact tension samples were oriented longitudinally with respect to the forging axis and had a thickness of 1.27 cm (0.5 in). These samples were polished to a 6 μm finish so that crack propagation could be observed during pre-cracking. Testing was performed using a servo-hydraulic load-frame machince with a digital controller. The load line displacement was obtained using a clip gauge, which has a gauge length of 0.254 cm (0.1 inch) and a range of 0.381 cm (0.15 inch). The compact-tension samples were fatigue pre-cracked at 20 Hz frequency with a stress ratio (R ratio) of 0.1. The peak load was established at 4.89 kN (1.1 kips) and maintained until crack initiation was detected. Following pre-cracking, side grooves of a depth of 20% of the total width, were added to the samples. The side-grooved samples were then loaded at a cross-head speed of 0.0013 cm s^{-1} (0.0005 inches s^{-1}) until fracture occurred. Two samples were tested for each over-aged heat treatment condition.

Additional three-point bend measurements were made on subsize samples using a screw-driven machine. The dimensions of the subsized three point bend samples were determined by the maximum decarburizing sample size. The corresponding dimensions of the samples were 20 mm in length, 5 mm in width, and 2.5 mm in thickness. EDM was used to cut a starter notch, with a width of 0.025 mm and a length of 1.125 mm, at the center of the 20 mm $\times$ 2.5 mm face. These samples were fatigue pre-cracked at 10 Hz frequency at a stress ratio (R ratio) of 0.1. The samples were tested using a cross-head speed of 0.00083 cm s^{-1}.

Optical and scanning electron microscopy (SEM) were employed to characterize the microstructures. Optical microscopy determined the general microstructure and the grain size, as well as variations in microstructures produced by composition gradients. The samples were polished a 1 μm surface finish. A sodium-metabisulfite etchant (167 ml H_2O, 33 ml HCl, 0.5 g $Na_2S_2O_5$) was used to revealed the martensitic structure within the prior-austenitic grains. A 10% Nital etchant was used to investigate the carbide structures. The fracture surfaces were characterized using a cold field emission scanning electron microscope (cFEG-SEM) with a energy dispersive spectroscopy (EDS) detector.

The corrosion behavior was evaluated using anodic polarization measurements. An electrode was soldered to the sample before mounting in epoxy. The exposed surface area was polished to a 1 μm and measured. A computer controlled potentiostat was used to measure the anodic polarization curves in derated solutions. For consistency with the previously obtained polarization data [7], the materials were tested in aqueous solutions of 1% sucrose (for conductivity) and 3.5% NaCl with pH = 7. The free corrosion potential was established by allowing the system to reach a steady-state conditions after sitting for 30 minutes. The anodic potential was scanned at a sweep rate of 2 mV s^{-1} continuously recording potential and current.

Salt-spray corrosion testing was conducted following the ASTM standard B117 [8]. Before testing, the samples were weighed to the nearest 0.0001 g and the exposed surface area was measured. The samples were polished to a 600 grit finish and cleaned with acetone. Then the samples were suspended in a fog chamber for a total of 48 h and were exposed to cycles of alternating environmental conditions of 2 h at 20 °C with a 5% salt spray solution and then 1 h dry heat at 30 ± 1 °C. After exposure, the samples were again weighed to determine a corrosion rate and the surface corrosion products were noted. The corrosion rate, R, is calculated using the expression:

$$R = \frac{8.7610^4 w}{\text{mm yr}^{-1}}, \tag{1}$$

where w is the measured weight loss in g, ρ is the density of the specimen in g cm^{-3}, a is the surface area exposed in cm, and t is the exposure time in hours. The presented corrosion rates serve as a preliminary analysis of the corrosion behavior of the materials as only two data points were collected for each sample.

3. Characterization of prototype (results)

The first step in evaluating the new alloy (CS62) was the characterization of the core material to determine the correct processing conditions of the forged material. While the case material properties are more important than the core properties, the correct processing of the core material must be established before carburizing the material to evaluate the case material properties and processing conditions. To assist in the characterization of the prototype, the Thermo-Calc [9] and DICTRA [10] software programs helped correlate observed microstructures to processing and material properties and aided in process optimization.

3.1. Core material

The measurement of the M_s temperature is the first step in the core material evaluation. Dilatometry determined a M_s temperature of 291 °C ± 15 °C, and an A_s temperature of 761 °C ± 10 °C. The temperature at which the free energy of the FCC phase equals the free energy of the BCC phase, the T_0 temperature, was calculated 16 degrees lower than the experimental T_0 of 521 °C. Figure 2 presents the recorded dilatometry curves, along with the optical microscopy of the quenched microstructure revealing the desired martensitic structure. In addtion, the observed microstructure showed no evidence of large segregation ratios, which would have resulted in bands of the martensitic laths corresponding to the composition variations.

Previous work [11] showed that optimizing the solution treatment temperature (T_s) maximizes the fracture toughness of an alloy. The optimal 1 h T_s is determined by the processing that produces the maximum hardness for the smallest grain size. When all of the carbon is in the FCC solid solution the hardness, measured after quenching, will level off with increasing T_s, but the grain size will continue to increase. The solution treatments were followed by an oil and liquid N_2 quenching to produce a martensitic transformation. The material was then tempered at 200 °C for 1 h (Stage I) to reduce quenching variations effects. Figure 3(a) shows the hardness dependence on temperature and Fig. 3(b) depicts the corresponding grain size dependence. After reaching a peak hardness of R_c 51.3 for a T_s of 1050 °C, the hardness leveled-off with increasing T_s, suggesting the full dissolution of the carbides. At the optimal T_s

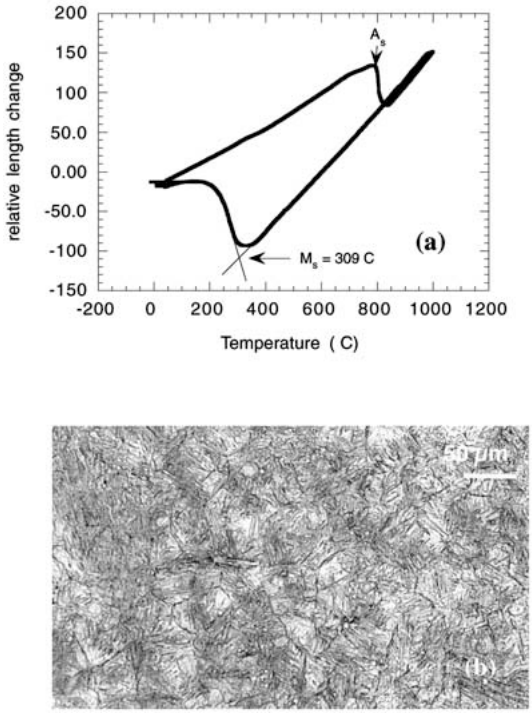

Figure 2. (a) Dilatometry curve representing the martensitc transformation. (b) Optical micrograph of the lath martensitic microstructure produced upon quenching from a T_s of 1050 °C.

of 1050 °C, the grain size is 30 μm, using the mean linear intercept method. For comparison, the commercial carburizing stainless steel, Pyrowear 675, has a solution treatment of 1050 °C for 1.5 h and the prototype 1605-8B alloy has a solution treatment of 1050 °C for 1 h. The optimized solution treatment for CS62 is also similar to that of an earlier stainless prototype, NASA1, which had an optimized solution treatment of 1150 °C for 1 h. The higher optimal solution temperature for the NASA1 alloy is attributed to its higher carbon (0.30 wt.% C) and vanadium contents (0.25 wt.% V) [7].

The secondary-hardening tempering response was investigated at three different temperatures: 510 °C, 482 °C, and 450 °C. At 510 °C only monotonic softening was observed, as demonstrated in Fig. 4. A broad peak hardness level at R_c 53.5 was observed at 482 °C. At 450 °C, peak hardness was not established after 24 h of tempering. Consequently, 482 °C, the assumed tempering temperature in the design calculations [2], was confirmed as an acceptable tempering temperature.

The fracture toughness, determined by K_{IC} testing, was characterized as a function of tempering time at 482 °C. Two slightly overaged conditions were chosen: 16 h and 22 h. Both conditions failed to maintain stable crack growth during pre-cracking: unstable crack growth was initiated after the fatigue pre-crack had grown to 75% of its desired length. Although a valid K_{IC} could not be ascertained for either the 16 h or 22 h tempered conditions, the fracture surfaces were evaluated to assess the fracture mechanisms and to estimate the toughness levels. The validity of the fracture surface evaluation to determine the active fracture mechanism in plane strain is based on the previous work developing the Stretch Zone Width (SZW) technique [12–14]. It was observed that the fracture surface just ahead of the SZW is

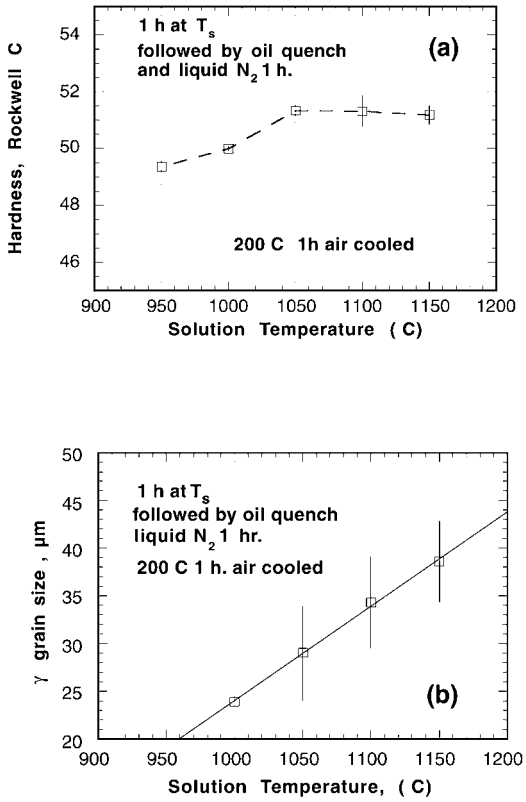

Figure 3. (a) Hardness as a function of solution temperature. (b) Grain size as a function of solution temperature.

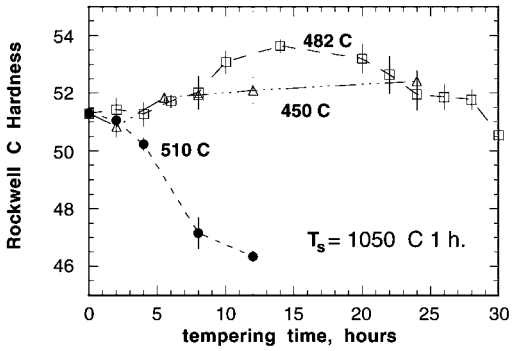

Figure 4. Tempering response at 510 °C, 482 °C, and 450 °C.

indicative of the initial fracture mechanism under plane strain constraints. SEM examination of the fracture surfaces, just beyond the fatigue pre-crack, reveal quasi-cleavage surfaces with signs of intergranular embrittlement, Fig. 5. The intergranular facets have a diameter of approximately 30 μm, which corresponded to the average grain size achieved after the 1050 °C solution treatment.

The underlying brittle failure modes achieved using secondary-hardening conditions did not meet the design objectives for the ductile fracture criteria. This was not completely unexpected. As noted earlier the processing of the alloy was not as clean as desired, and the core

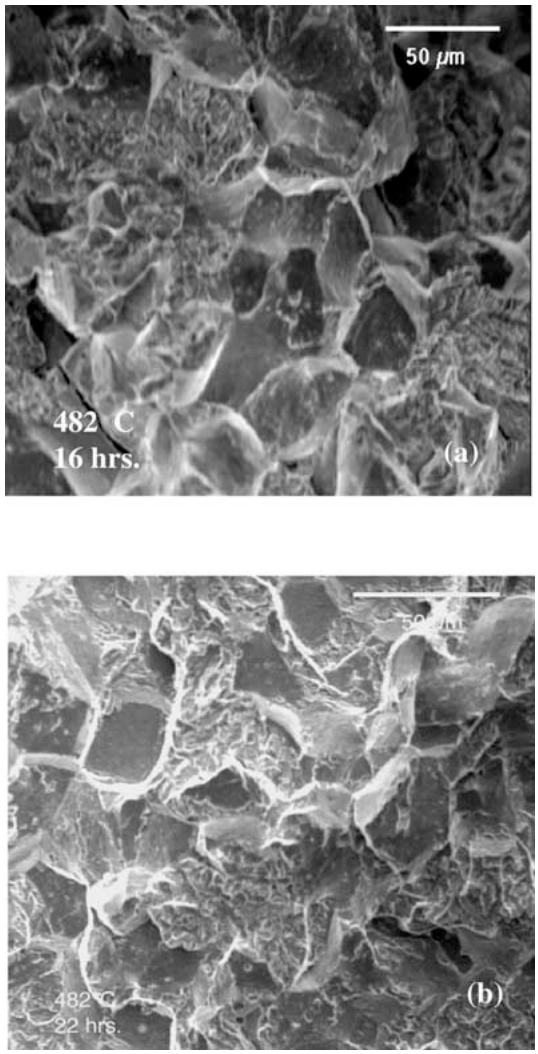

Figure 5. SEM micrographs of the fracture surfaces observed after (a) 16 h and (b) 22 h of tempering at 482 °C.

composition was designed that the carbon content could be adjusted to achieve the desired toughness without significantly impacting the case microstructure design. Further investigation of the fracture mechanisms as a function of heat treatment and composition was worthy of study to determine how future modeling efforts could be improved.

Evaluation of the fracture mechanisms as a function of heat treatment include investigation of the stage I tempering conditions. After tempering for 1 h at 200 °C, a K_{IC} of 68 ± 1.5 MPa$\sqrt{\text{m}}$ (62 ± 1.5 ksi$\sqrt{\text{in}}$) at R_c 52 was measured and a ductile fracture surface was observed, as seen in Fig. 6. This result at R_c 52, which is only 1 R_c point below the secondary-hardening conditions examined, indicated that with a fine ϵ-carbide strengthening dispersion the alloy has sufficient Ni content to resist cleavage fracture at room temperature. It should be noted in Fig. 6 that there are some large voids, approximately 25 μm in diameter, which can be attributed to oxide inclusions resulting from the higher than desired oxygen content in the experimental heat.

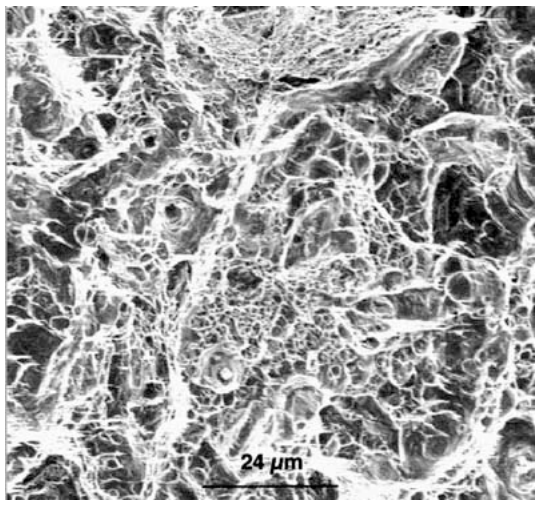

Figure 6. SEM micrograph of the ductile fracture surface produced after tempering at 200 °C for 1 h.

Table 2. Heat treating conditions for the decarburized samples

Alloy	Homogenization	Solution treatment	Tempering
CS62 – 0 h	NA	1050 °C 1h	200 °C 1 h
CS62 8 h	1100 °C 10 h	1050 °C 1 h	510 °C 2 h
			482 °C 6 h
CS62 – 10 h	1050 °C 20 h	1100 °C 0.5 h	510 °C 2 h
			482 °C 6 h
CS62 – 20 h	1050 °C 20 h	1100 °C 0.5 h	510 °C 2 h
			482 °C 6 h
1605-8B 0 h	NA	1050 °C 1h	200 °C 1 h
1605-8B 8 h	1100 °C 10 h	1050 °C 1 h	510 °C 2 h
			482 °C 6 h
1605-8B 10 h	1050 °C 20 h	1100 °C 0.5 h	510 °C 1 h
1605-8B 20 h	1050 °C 20 h	1100 °C 0.5 h	510 °C 1 h

The reduction in fracture-toughness associated with secondary-hardening is most likely the result of the loss of grain boundary cohesion. Spaulding [15] evaluated the P and S segregation and decarburization embrittlement during secondary hardening of the 1605 model alloys and a prototype gear steel. The study concluded that the critical Griffith work for interfacial separation depended on the hardness level and demonstrated that ductile fracture modes could be obtained with reduced carbon levels. Thus, to determine the necessary reduction in alloy hardness to change the fracture mechanism in the secondary-hardened condition, decarburization studies were conducted.

Based on DICTRA simulations [16], decarburization experiments were performed on CS62 and 1605-8B in wet hydrogen for 8 h, 10 h, and 20 h. Following decarburization, the final vacuum homogenization treatments were also guided by DICTRA simulations. For the 8 h

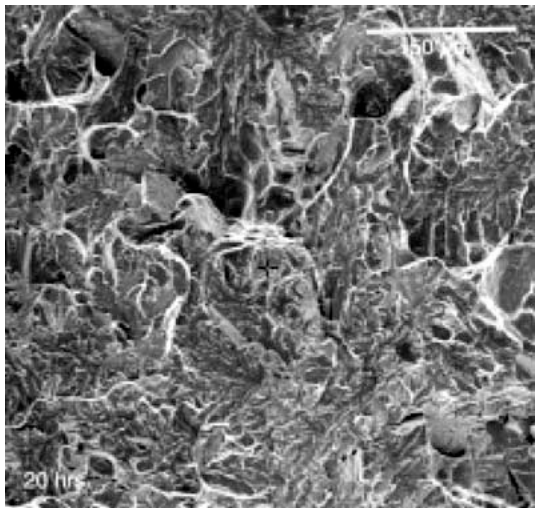

Figure 7. Fracture surface of CS1 decarburized for 20 h at 1100 °C (0.14 wt.% C).

decarburized samples, homogenization was completed at 1100 °C for 10 h. The 10 h and 20 h decarburized samples were homogenized for 20 h at 1050 °C. Following solution treatment and tempering (see Table 2 for specific conditions), the subsized 3-point bend samples were pre-cracked and fractured.

The results of the fracture testing were evaluated with the understanding that the fixed subsized specimen geometry could result in varying crack tip stress states with decreasing hardness levels, making fracture analysis difficult. In addition to the constraints of the subsize specimen geometry, the fracture-toughness analysis was limited by the higher than desired oxide content. The following analysis is intended to provide a qualitative description of the fracture mechanisms present in the lower carbon version of the alloy. It is accepted that for the fixed sample geometry, as the crack grows in a ductile material the plastic zone may exceed the sample width and plane strain conditions will not be maintained. However, the initial crack will form under plane strain conditions, so that fractorgraphy at the beginning of stable crack growth will be representative of the initial acting fracture mechanism in plane strain.

After 8 h of decarburization, both CS62 (480 Vickers Hardness Number (VHN)) and 1605-8B (373 VHN) had quasi-cleavage fracture surfaces. Ten and 20 h of decarburization reduced the carbon content of 1605-8B enough to produce a ductile fracture at less than 290 VHN. Unfortunately, 20 h of decarburization was not sufficient to produce a ductile fracture in CS62 with a 437 VHN. However, the fracture surface in Fig. 7 reveals some evidence of a more ductile fracture mode with little evidence of intergranular fracture. The microhardness profiles across the decarburized samples were measured and the strengthening model [17] was used to estimate the carbon level. The relatively flat hardness profiles indicated that the homogenization treatments were successful. The hardness levels, estimated carbon contents, and estimated K_{IC} values are given in Table 3.

Due to the small size of the samples, the estimated K_{IC} values require scaling to better represent values obtained from standard size samples. Using the work of Bergstrom [18] and calibrating the K_{IC} measured on the original CS62 material with a standard thickness (K_{IC} standard = 68 MPa$\sqrt{\text{m}}$: K_{IC} subsize = 132 MPa$\sqrt{\text{m}}$), the experimental K_Q values were scaled using a factor of 0.5 to predict a more representative K_{IC} estimate for screening

Table 3. Results of decarburization experiments

Alloy and condition (h of decarb.)	Hardness (VHN)	Estimated C, wt.%	Measured K_Q	Estimated K_{IC} MPa$\sqrt{m}$
CS62 – 0 h	590	0.21	132	66
CS62 – 8 h	480	0.17	NA	NA
CS62 – 10 h	473	0.17	NA	NA
CS62 20 h	437	0.14	55.5	27.7
1605-8B – 0 h	585	0.24	124	62.1
1605-8B 8 h	373	0.10	87.4	43.6
1605-8B – 10 h	290	0.04	140	70*
1605-8B – 20 h	287	0.04	122	61*

*Estimated value; unable to break samples using Sintech.

purposes. Figure 8(a) shows the measured hardness decreasing as a function of decarburization time. From Fig. 8, it is estimated that 45 h of decarburizing at 1100 °C is required to reduce the carbon level of the design composition to 0.05 wt.% C, and thus produce a ductile fracture condition after secondary-hardening.

Combining the results of the various investigations of the fracture mechanisms resulting from secondary-hardening treatments, a mechanism map of the dominating fracture modes defined by the carbon content and hardness was constructed, as seen in Fig. 9. The data represented on the map included the decarburization experiments on CS62 and 1605-8B and the overaging experiments of CS62. The fracture map is divided into three regions. Above a hardness level of 525 VHN intergranular fracture dominates. Intergranular fracture also occurs at low hardness levels, to the right of the line:

$$\text{VHN} = 1527 \cdot (\text{wt.\%C}) + 175. \tag{2}$$

To the left of the intergranular boundary and between the hardness levels of 375 VHN and 575 VHN is a region of quasi-cleavage. At hardness levels below 375 VHN and carbon contents to the left of the intergranular boundary ($\approx <$ 0.10 wt.% C), ductile fracture mechanisms prevail.

The two regions of intergranular fracture indicate two different mechanisms. Intergranular fracture occurring at high carbon and hardness is represented by standard overaged tempering treatments of 1605-8B and CS62. Spaulding's work [15] showed that depletion of cohesion-enhancing C at the grain boundaries can cause for intergranular fracture at hardness levels greater than 450 VHN. The lower region of intergranular fracture is characterized by the long time overaging experiments on CS62, where the segregation of P and S impurities is likely to be the cause of the lost grain boundary cohesion.

The fracture mechanism map of Fig. 9 suggests that to achieve a ductile fracture mode using secondary-hardening, the carbon content of the prototype composition must be decreased to approximately 0.05 wt.% C. Such a lower carbon content alloy is currently under evaluation. The upper region of intergranular fracture indicates that fracture surface analysis of the grain boundaries is needed to determine if the boron additions, which were added to improve grain-boundary cohesion, are present, or if boron was oxidized during processing.

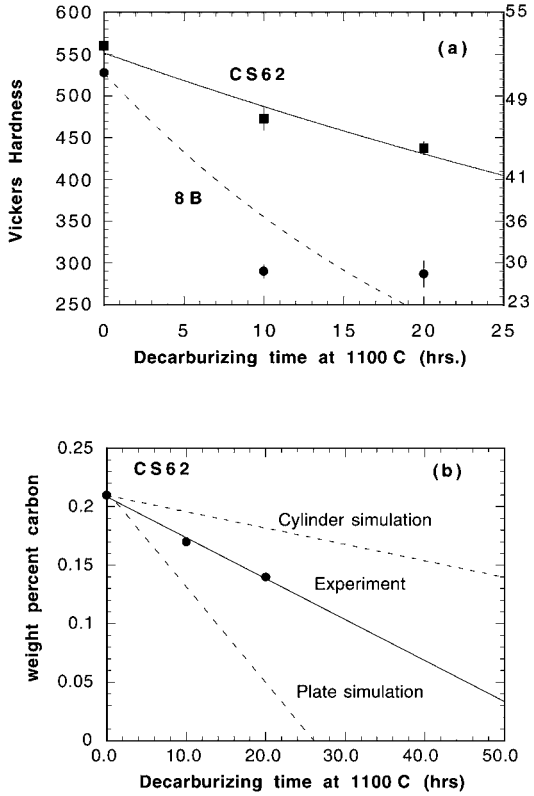

Figure 8. (a) Hardness as a function of decarburizing time a 1100 °C for alloys 1605-8B and CS62. (b) Alloy carbon content as a function of decarburizing time for CS62. Experimental carbon concentration estimates are compared to the predictions of the DICTRA simulations for the plate and cylinder geometries.

3.2. CASE MATERIAL

Optimal carburizing would produce 0.48 wt.% surface C with a 1 mm case depth. Using industrial gas-carburizing practices performed by Caterpillar Inc., pre-oxidation at 900 °C was followed by gas-carburizing for 5 h at 927 °C at nominal 1.0 surface carbon potential to produce a 1.6 wt.% surface carbon with 1.5 mm case depth, as shown Fig. 10. The higher than nominal surface carbon content is predicted for the high Cr level. To produce a case without primary carbides the surface carbon was reduced. The computed equilibrium carbon isopleth indicates that at 927 °C M_7C_3 carbides are present. The predicted carbon distributions in the FCC matrix at the carburizing and solution treatment temperatures are shown in Fig. 11 and the corresponding phase fields are shown in Fig. 12.

Diffusion treatments were used to reduce the surface carbon and to dissolve the primary carbides. DICTRA simulations were again used as a guide in determining the best treatment. At 1175 °C, the carbon solubility in the FCC phase is 0.7 wt.% C. Using the measured carbon profile after carburizing and assuming an equilibrium spheroidal M_7C_3 carbide distribution, Fig. 13 presents the DICTRA simulations of the austenite carbon diffusion process at 1175 °C in the two-phase field. The simulation predicts that after 2 h a 0.65 wt.% surface carbon level should be achieved and the primary carbides would be dissolved at equilibrium. This diffusion step was performed followed by oil and liquid N_2 quenching and a 200 °C 1 h temper.

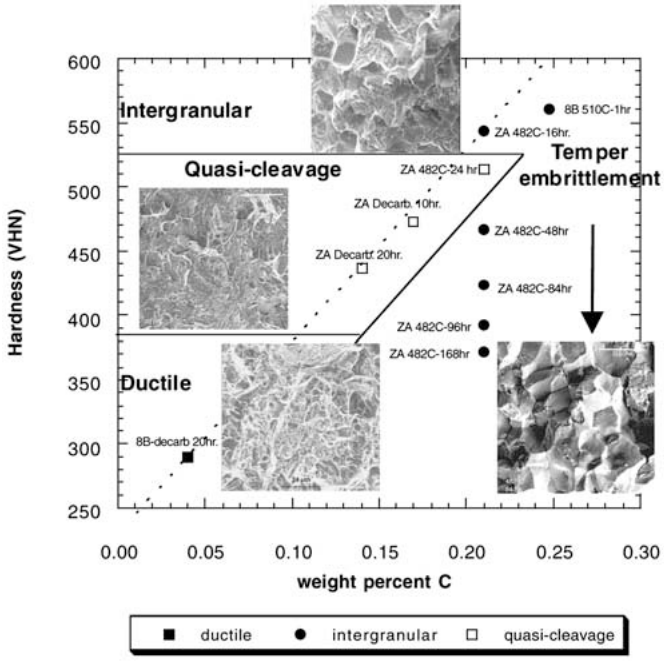

Figure 9. Fracture mechanism map defining the region of intergranular, quasi-cleavage, and ductile fracture by the carbon content and hardness. The fracture surfaces are representative of the different fracture modes.

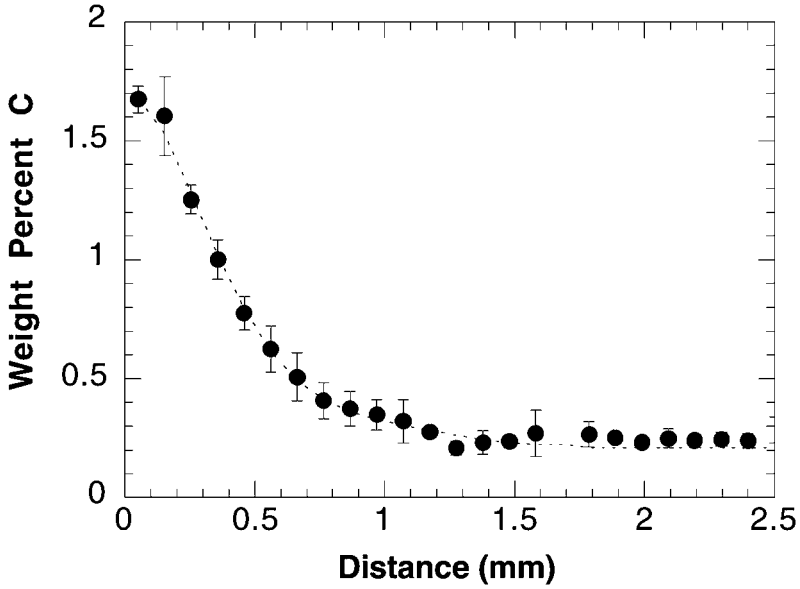

Figure 10. Measured carbon profile after initial carburizing at 927 °C for 5 h at nominal 1.0 surface carbon potential.

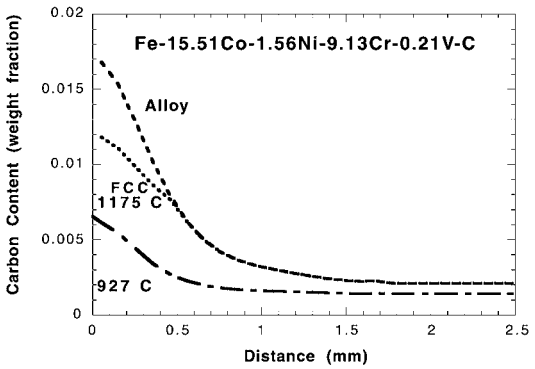

Figure 11. Computed carbon distribution in matrix at 927 °C and 1175 °C assuming equilibrium with the M_7C_3 carbide.

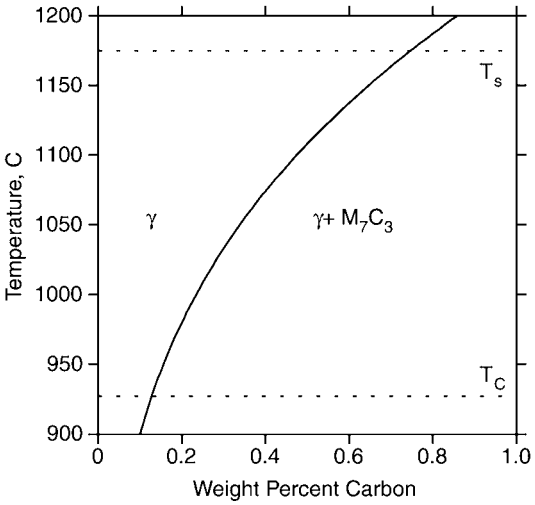

Figure 12. Carbon isopleth for CS62. Dashed lines denote the carburizing (T_c) and solution (T_s) temperatures.

The resulting hardness profile with a surface hardness of 790 VHN is shown in Fig. 14(a). Figure 14(b) show the hardness profile after secondary hardening at 482 °C for 18 h and indicates a measured surface hardness of 816 VHN. Secondary hardening produced slightly higher case and core hardnesses. Both profiles show a large case depth (≈3 mm) due to the long carbon diffusion step.

Optical microscopy of the case microstructure confirms a martensitic matrix, as seen in Fig. 15. The amount of retained austenite and plate martensite increases toward the surface. Microscopy also shows the presence of some primary carbides (M_7C_3) in the first 250 μm of the case, indicating that equilibrium at 1175 °C was not fully established.

Although the measured case hardness met the original property objective, detailed analysis of the hardness and carbon profiles shows quantitative discrepancies with the design model predictions. A maximum hardness of 816 VHN is obtained at a case depth of 200 μm with the presence of some primary carbides. The maximum hardness achieved without primary carbides is 800 VHN at 300 μm. The DICTRA carburization simulation predicted a 0.625 wt.% C composition at a case depth of 200 μm and 0.62 wt.% C composition at 300 μm. To evaluate the design strengthening model, the DICTRA simulations were used to determine

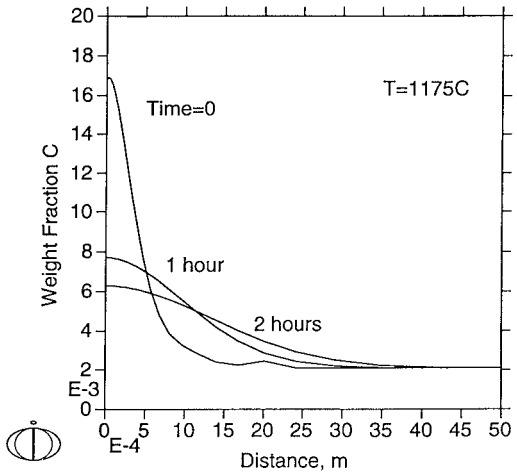

Figure 13. DICTRA simulation at 1175 °C for the diffusion of the carbon distribution produced after carburizing at 927 °C.

the case depth at which the design carbon content (0.48 wt.%) was obtained. The hardness at this case depth of 1.25 mm is 775 VHN, 50 points below the design value of 825 VHN. The slightly lower than desired hardness can be attributed to the M_2C driving force being lower than the original target value, producing a larger M_2C particle size with less efficient strengthening.

The fine size scale associated with the alloy M_2C carbides precipitated during secondary-hardening should provide higher resistance to fatigue and wear corrosion compared to alloys that use primary carbides as a strengthening dispersion. For comparison with such an alloy, the commercial Pyrowear 675 alloy was studied. Initial carburizing of the primary carbide strengthened alloy using pack-carburizing highlights a large difference in alloy processability. Despite using various slow cooling methods from the recommended carburizing temperature of 871 °C a crack-free surface could not be obtained, Fig. 16. Modeling indicates that the surface cracks were generated from the residual tensile stresses produced by a M_s profile that reverses directions with increasing carbon, Fig. 17(a). For comparison, the desirable montonic M_s temperature profile for CS62 is shown in Fig. 17(b). For the Pyrowear 675 alloy, the combination of low matrix carbon and high matrix Cr results in an increasing M_s temperature as the carbon content increases. The additional alloy C from carburizing removes Cr from the matrix to form M_7C_3 carbides. This decrease of matrix Cr increases the M_s temperature. Figure 18 depicts the C isopleth of this primary carbide strengthened alloy and shows that both the carburizing and solutionizing temperatures correspond to multiphase regions.

Case cracking of the primary carbide strengthened alloy was avoided when a more controlled carburizing method was utilized. Gas-carburizing for 24 h at 871 °C at a nominal 0.7 surface carbon potential, by MRC Bearing Corp., produced a crack-free case. Both carburizing processes were followed by the standard solutionizing (1050 °C for 1.5 h) and tempering (510 °C for 4 h) procedures for the alloy. This heat treatment and carburizing process produced a hardness of R_c 60 at case depth of 0.11 cm and a R_c 50 at 0.19 cm.

Anodic polarization measurements in 1% sucrose and 3.5% NaCl aqueous solutions were made on the core material of Pyrowear 675 and CS62 and the carburized CS62. The measure-

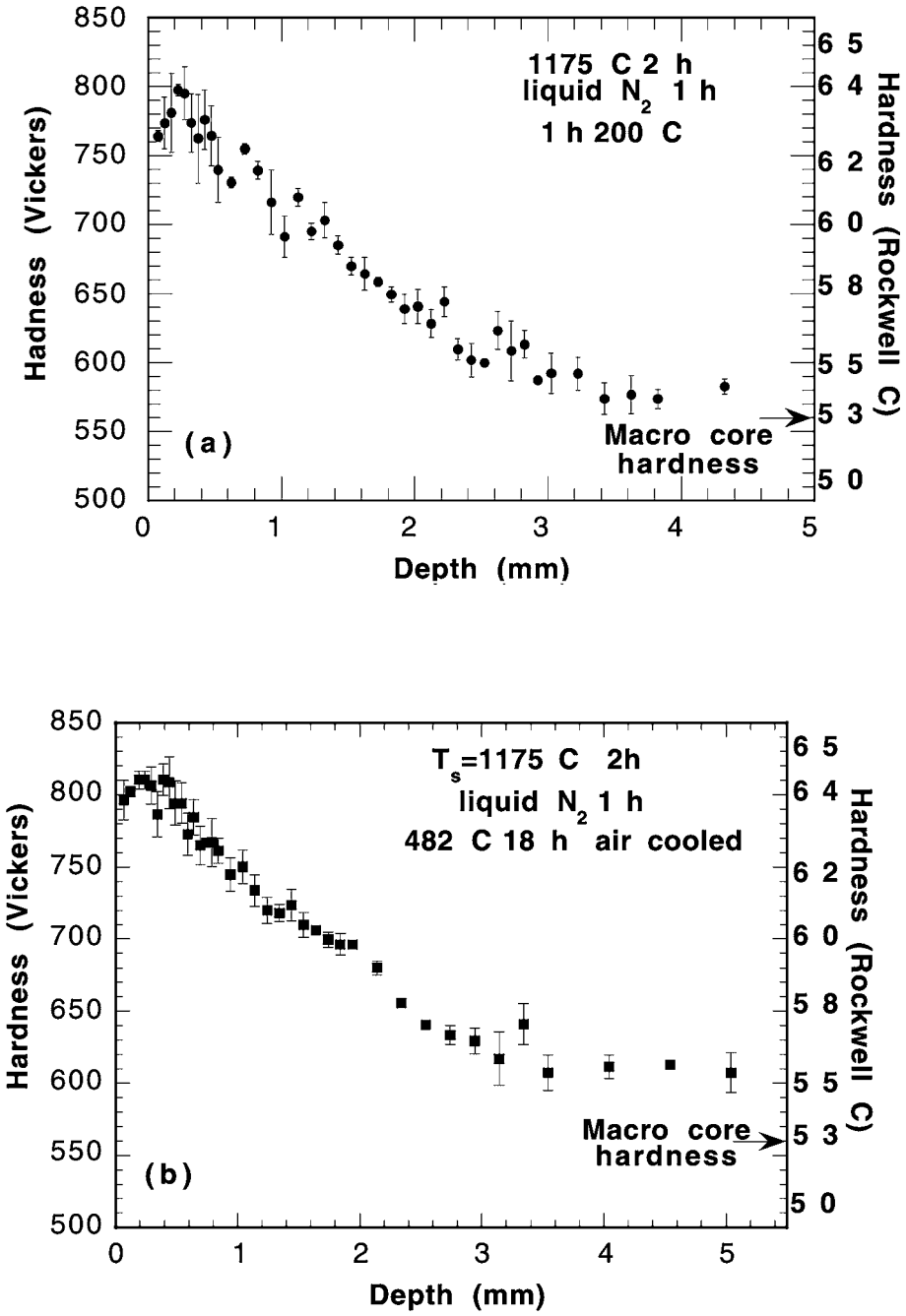

Figure 14. Hardness profiles after (a) after Stage I tempering at 200 °C for 1 h and (b) after secondary-hardening at 482 °C for 18 h.

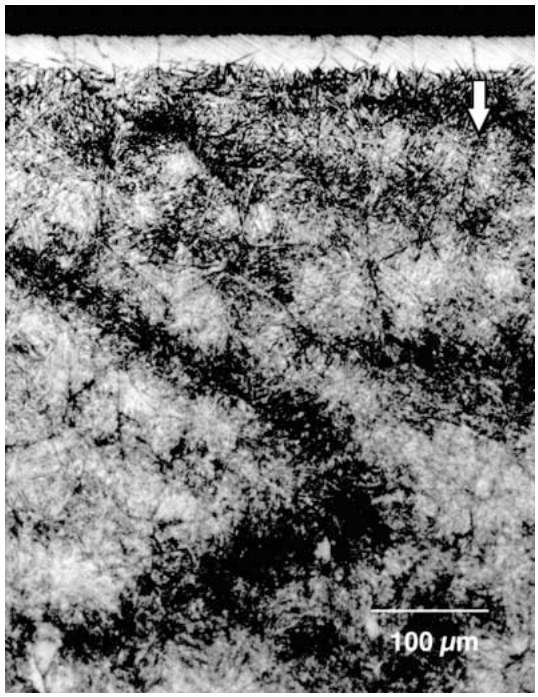

Figure 15. Optical micrograph of the case microstructure after 2 h at 1175 °C followed by 18 h at 482 °C. Arrow denotes direction of carbon diffusion.

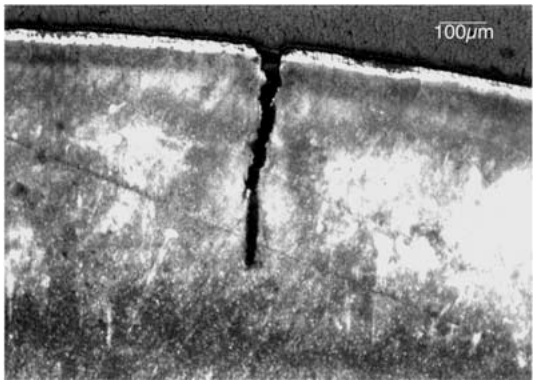

Figure 16. Case-cracking observed after pack-carburizing Pyrowear675.

ments were compared to previous measurements made on 440C and the NASA1 prototype stainless bearing steel [7]. Figure 19(a) compares the anodic polarization resistance of the various monolithic alloys and Fig. 19(b) compares the core and case material of CS62. The core material of CS62 behaved similarly to the core material of Pyrowear 675. Pyrowear 675, NASA1 and the case and core material of CS62 all surpass the anodic polarization curve of 440C. Figure 19(b) shows the remarkable result that carburization of CS62 causes only a slight reduction in the corrosion resistance compared to the core material. This suggests that the fine-scale strengthening dispersion does not remove a signifcant concentration of Cr from the matrix and thus, the Cr is still available to contribute to passive film formation.

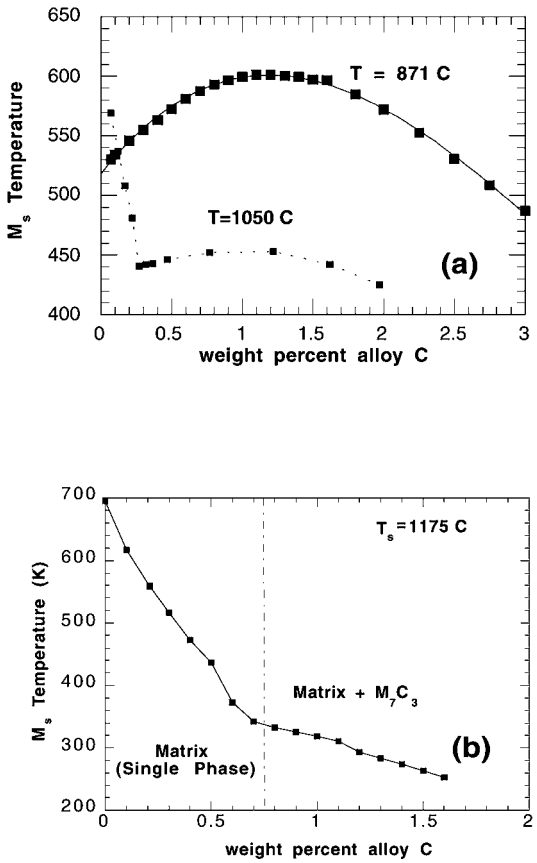

Figure 17. (a) Predicted M_S temperature distribution corresponding to the Pyrowear675 matrix carbon content at the carburizing and solutionizing temperatures. (b) Predicted M_S temperature distribution for CS62 at the solution temperature of 1175 °C.

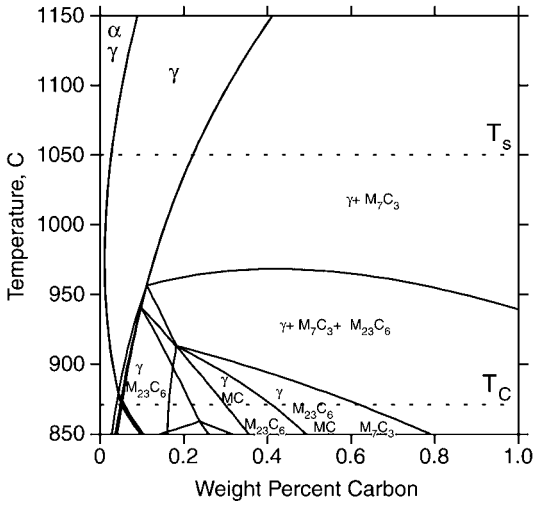

Figure 18. Computed carbon-isopleth for Pyrowear675. Dashed lines represent the carburizing (T_c) and solutionzing (T_s) temperatures.

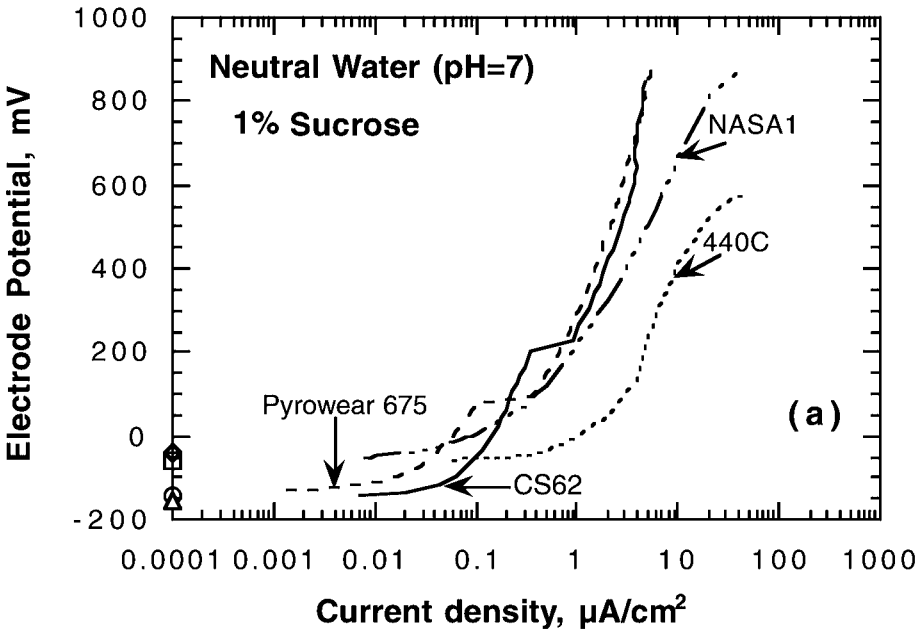

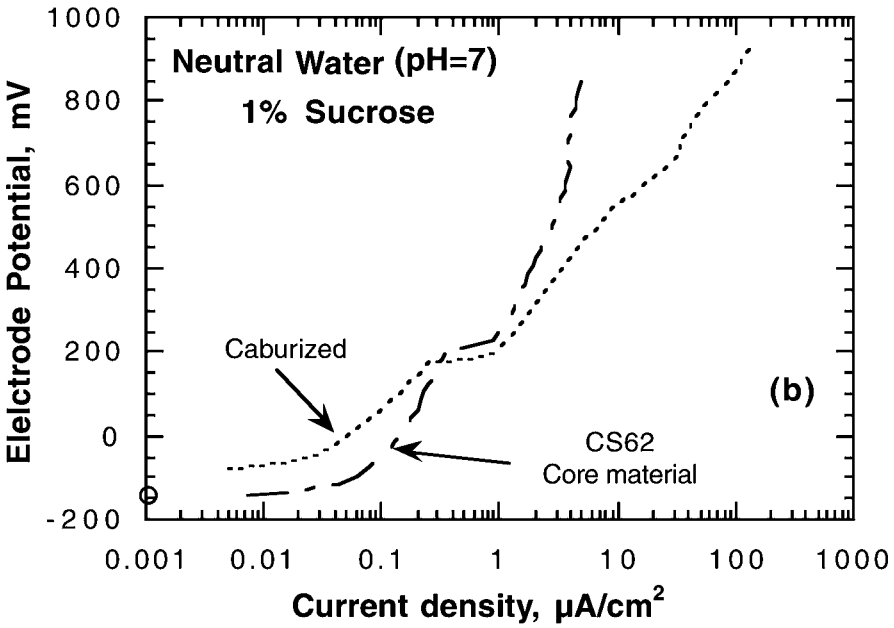

Figure 19. (a) Anodic polarization measurements in 1% sucrose solution for monolithic alloys and (b) comparison of the behavior of the case and core material of CS62. The E_{corr} values are represented by the open symbols where o = CS62, □ = 440C, △ = Pyrowear 675 and ◊ = NASAI

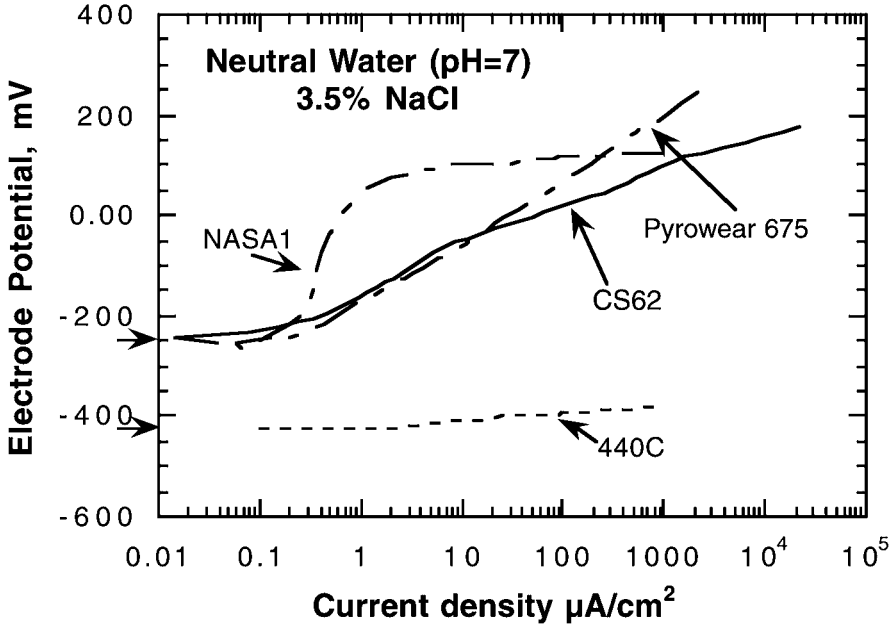

Figure 20. Anodic polarization measurements in 3.5% NaCl solution for monolithic alloys.

Table 4. Corrosion rates after salt-spray testing

Alloy	Corrosion rate, mm yr^{-1}
CS62	0.00256
CS62-carburized	0.0234
Pyrowear 675	0.00663
Pyrowear 675-carburized	0.0747

With testing in the 3.5% NaCl solution, Fig. 20, NASA1 exhibits the superior resistance. The 440C alloy showed no distinguishable evidence of passivation, as evident by the shallow slope of the potential versus current line, in contrast to the behavior of Pyrowear 675 and CS62 alloys. At high potentials where pitting occurs, the Mo-bearing Pyrowear 675 has slightly better performance than CS62. However, both Pyrowear 675 and CS62 show only very small passivating regions and further experimental work is needed to clarify the electrochemical reactions. Carburized Pyrowear 675 was not tested as a crack-free surface was not available at the time of testing. Due to the high content of primary carbides in the carburized condition, significant degradation of the corrosion resistance is expected.

Salt-spray testing illustrated the superior performance of the prototype composition as seen in the measured corrosion rates, Table 4. The guidelines given by Fontana [19] for corrosion rates in ferrous and nickel-based alloys hold that corrosion rates <0.0254 mm yr^{-1} are 'outstanding' and rates between 0.0254 mm yr^{-1} and 0.127 mm yr^{-1} are 'excellent'. The carburized sample of Pyrowear 675 test is affected by case cracking. It was also noted that the

Table 5. Predicted and measured properties of the prototype composition

Property	Design	Measured
Core Properties		
M_s temperature, °C	300	291
Hardness at 50% M_2C completion	575 VHN ($R_c \sim 54$)	R_c 53.5
Hardness stage I	–	R_c 52
Solution temperature, °C	–	1050
grain size at T_s for 1 h		30 μm
K_{IC} MPa$\sqrt{\text{m}}$	50	68 (Stage I)
		29 (Stage IV)
Corrosion rate, mm yr^{-1}	–	0.0256
Case Properties		
Matrix structure	martensitic	martensitic
Hardness at 50% M_2C completion	825 VHN	816 VHN R_c 64.5
Hardness stage I	–	800 VHN R_c 64
Solution temperature, °C	1100	1175
Corrosion rate, mm yr^{-1}	<0.051	0.0234

surface of carburized Pyrowear 675 was covered with black oxide scale after testing. No such scale was formed on the carburized CS62.

Initial rolling contact fatigue (RCF) testing using a 3 ball-on-rod method indicates that at a contact stress of 5.42 GPa (786 ksi) carburzied CS62 has a fatigue life equivalent to M50, a commerical high temperature monolithic bearing steel. Wells et al. [20] performed similar RCF testing using the same contact stress of 5.42 GPa and compared the M50 alloy to carburised Pyrowear 675. With an optimal heat treatment, the B50 lifetime (Weibull distribution for 50% accumulated failure) of Pyrowear 675 was five times greater than M50 .

4. Discussion

Using a systems approach to computational materials design, a carburizable, secondary-hardening, martensitic stainless steel was designed, which meet all of the case material property objectives, requires only thermal processing, and appears capable of meeting all of its property objectives. Establishing the desired property objectives, by analysis of existing bearing, secondary-hardening and stainless steels, a quantitative conceptual design was embodied by developing and integrating design models for the martensitic transformation behavior, the coherent M_2C carbide precipitation strengthening, the formation and stability of passivating oxide films, and the microsegregation occurring during solidification processing.

The design properties are compared to the measured properties in Table 5. A case surface hardness of R_c 64.5 was obtained without the use of extensive primary carbides. The benefit of this microstructure was illustrated by the difficulty in processing the Pyrowear 675 alloy, which uses primary carbides to achieve its R_c 64 surface hardness. When pack-carburizing, the formation of primary carbides resulted in a tensile stress at the surface as the M_s temperature distribution was reversed. The martensitic case microstructure free of primary carbides in

CS62 improved the RCF life as supported by preliminary studies showing the RCF life of carburized CS62 equilivalent to the M50 bearing steel.

The case diffusion temperature was higher than desired due to limitations of standard industrial carburizing conditions. With better control of the carburizing conditions the diffusion temperature could be decreased to the design solution temperature while achieving a reasonable case depth.

Consistent with model predictions of alloying effects on Cr partitioning to the passive film, anodic polarization measurements and salt-spray testing demonstrated the success of the 9Cr (CS62) alloy to achieve similar corrosion properties as traditional 12–13Cr steels. Anodic polarization measurements in 1% sucrose and 3.5% NaCl show similar resistance for both the core material of CS62 and the 13Cr alloy, Pyrowear 675. Both alloys exceed the corrosion resistance of 440C stainless bearing alloy. In the 3.5% NaCl solution the NASA1 alloy (12Cr–25Co) has the best resistance. However, further anodic polarization measurements are needed to clarify electrochemical reactions.

Measured corrosion rates from salt-spray testing also illustrate the excellent performance of CS62. Quantitative comparison of the carburized CS62 and carburized Pyrowear 675 material was hampered by case cracking of the later. However, carburized CS62 should have superior corrosion resistance to carburized Pyrowear 675, as the case CS62 does not have a large fraction of primary carbides depleting the matrix of Cr. This is supported by the demonstration that carburizing causes only a slight reduction in the corrosion resistance of CS62.

The evaluation of the core material included the measurement of the M_s temperature and the fracture toughness. For the received prototype composition, the measured M_s temperature is within 10 deg of the predicted temperature. The initial core hardness objective was achieved, with R_c 51.3 as-quenched hardness. The core fracture toughness objective was surpassed using Stage I tempering (200 °C, 1 h), $K_{IC} = 68$ MPa$\sqrt{\text{m}}$ at R_c52. In the secondary hardened condition, the fracture toughness at R_c 53 was similar to current bearing steels, $K_{IC} = 29$ MPa$\sqrt{\text{m}}$. Higher K_{IC} values are expected for cleaner alloy heats (< 0.008 wt.% O). The limited fracture toughness achieved with secondary hardening is primarily attributed to grain boundary embrittlement. Retaining the originally desired high core hardness of R_c 53 at 0.20 wt.% C in the secondary-hardening condition will require enhancement of grain boundary cohesion. Decarburization experiments indicate that a ductile core can be obtained by lowering the carbon content to 0.05 wt.% C corresponding to a core hardness of R_c 30.

Table 6 compares the properties of CS62, Pyrowear 675 and 440C. If used in the Stage I tempering conditions, CS62 surpasses in all properties. Although Pyrowear 675 has a much higher core fracture toughness, its core strength is much lower. Using CS62 as a secondary-hardening alloy, it has a fracture-toughness similar to 440C; however, it has a higher surface hardness, and should have greater dimensional stability as it has no primary carbides. CS62 should also have fewer solidification segregation problems than Pyrowear 675, which has 1.8 wt.% Mo and higher Cr. Microsegregation calculations show that the Mo has the greatest potential for segregation.

Reducing the core carbon level to achieve high-toughness with secondary-hardening in CS62 will require minimal change in the system of interactions depicted in Fig. 1. The case structure and composition met the desired properties objectives and is actually the more complex subsystem to design in the case/core system. Lowering the core carbon level will not alter the case composition, and will also increase the core M_s temperature, resulting in a desirable

Table 6. Properties of CS62, Pyrowear 675 and 440C

Property	CS62	Pyrowear 675	440C (monolithic alloy)
Matrix Cr (wt.%)	9 core/ 9 case	13 core/ 5 case	11 matrix / 17 alloy
Core hardness, R_c	52	40	60
Case hardness, R_c	64	64	60
Core fracture Toughness K_{IC} (MPa$\sqrt{\text{m}}$)	68 Stage I 29 Stage IV	150	20
Predicted y_{Cr} in oxide film	0.75	0.64	0.54
Corrosion rate, mm yr^{-1}	0.00256 (core) 0.0234 (carb.)	0.00663 (core) 0.0747 (carb)	NA

steeper M_s gradient in the case. The processing of the alloy should remain the same, as the case composition is unaltered.

While the models used were sufficient to design the current prototype, further modeling work will improve the accuracy of the models and increase variety of design applications to which the models can be applied. Current modeling of the martensitic transformation behavior emphasizes the prediction of the M_s temperature; however, future applications may require control of the martensitic morphology as well. For example, controlling the fraction of plate and lath martensite in the case of a carburized steel. Characterization of the design prototype highlighted the need for improved modeling capabilities describing fracture toughness. These improvements are most likely to come from quantam mechanics modeling of impurity-induced embrittlment, which provide insights into the electronic bonding of various impurities at the grain boundaries, and the implementation of these results into a design process. While current simplistic modeling of the aqueous corrosion resistance was sufficient for this application, a better understanding of the kinetic process is needed. Ideally, the aqueous corrosion modeling should include the diffusion simulation of the growing passive film and indicate the composition gradient in the passive film. As all of the models developed rely correlating material properties and processing to thermodynamic quantities and diffusion reactions, all the modeling efforts are enhanced with improved thermodynamic and diffusion mobility assessments.

5. Conclusions

By designing a case material which avoids the use of primary carbides and optimize the partitioning of Cr into the passivating oxide films for corrosion resistance, a carburizing, secondary-hardening, martensitic stainless steel was developed that maintains the strength levels of the 440C composition while increasing the aqueous corrosion resistance and fracture toughness. Although the development of CS62 was a three year process based on two previous prototypes, an important output was the development of transferable process kinetic and thermodynamic models. These models, defining the martensitic transformation behavior,

the precipitation of the coherent M2C strengthening dispersion, the microsegregation resulting from solidification processing, and the passivation behavior of oxide films formed, can now be used to design high performance stainless steels to meet the specific property requirements of a given application, as outlined in Part I [2] in the design objectives. The models developed are also useful in the design of other high performance ferrous alloys, such as high-performance aerospace gear steels. The same systems design strategy can also be applied to other materials, as already demonstrated by the design of case-hardenable polymer gears [21]. Thus, a systems design approach provides an efficient and organized methodology for computational materials design requiring far fewer experimental prototypes. Once the required design models are developed for a given system, the time and cost for alloy development can be greatly reduced.

Acknowledgements

This research was supported by a NSF Graduate Fellowship for CEC and was conducted as part of the multi-institutional Steel Research Group program. The authors thank Dr C. J. Kuehmann for assistance with the toughness and fatigue testing. Pyrowear675 was provided by Carpenter Technology. Alloy 1605-8B was produced by NKK Corporation, Japan. Gas-carburizing of the alloys was performed by Caterpillar Inc. and MRC Bearings Corp.

References

1. Jenkins, G.M., In Beishon, J. and Peters, G. (Eds.), Systems Behavior, Open University Press, Birmingham, UK, 1972, pp. 56–79.
2. Campbell, C.E. and Olson, G.B., J. Comput.-Aided Mat. Des, (2001)
3. Kuehmann, C.J., Olson, G.B., Wise, J.P. and Campbell, C., Northwestern University, U. S. Patent, #6,176.946, 2001.
4. Kuehmann, C.J. and Olson, G.B., In Hawbolt, E.B. (Eds.), International Symposium on Phase Transformations During the Thermal Mechanical Processing of Steel - Honouring Professor Jack Kirkaldy, The Metallugrical Society of the Canadian Institute of Mining Metallurgy and Petroleum, 1995, pp. 345–356.
5. CarTech, U.S. Patent 5,002,729, 1993.
6. Annual Book of ASTM Standards, Vol. 03.01, ASTM, Philadelphia, PA, 1997, pp. 413–443.
7. Stephenson, T.A., Campbell, C.E. and Olson, G.B., In Richmond, R.J. and Wu, S.T. (Eds.), Advanced Earth-to-Orbit Propulsion Technology, NASA Conference Publication 3174, 1992, pp. 299–307.
8. Annual Book of ASTM Standards, Vol. 02.05, ASTM, Philadelphia, PA, 1996, pp. 1–8.
9. Sundman, B., Jansson, B. and Andersson, J.O., CALPHAD, 9 (1985) 153.
10. Borgenstam, A., Engström, A., Höglund, L. and Ågren, J., J. Phase Equilibria, 21 (2000) 269.
11. Kuehmann, C.J., Doctoral dissertation, Northwestern University, 1994.
12. Amouzouvi, K.F. and Bassim, M.N., Mater. Sci. Eng., 55 (1982) 257.
13. Hoelzer, D.T., Ali, J.A. and Ebrahimi, F., Scr. Metall., 20 (1986) 1575.
14. Srinivas, M., Kamat, S.V. and Rao, P.R., J. Testing and Evaluation, 22 (1994) 302.
15. Spaulding, D., Doctoral dissertation, Northwestern University, Evanston, IL, 1995.
16. Campbell, C.E., Doctoral dissertation, Northwestern University, Evanston, IL, 1997.
17. Wise, J.P., Doctoral dissertation, Northwestern University, Evanston, IL, 1998.
18. Bergstrom, D., Doctoral dissertation, Northwestern University, Evanston, IL, 1996.
19. Fontana, M.G., Corrosion Engineering, McGraw-Hill, New York, 1986.
20. Well, M.G.H., Beck, J.C., Middleton, R.M., Huang, P.J., and Wert, D.E., Surf. Engineer., 15 (1999) 321.
21. D'Oyen, R., Doctoral dissertation, Northwestern University, Evanston, IL, 1997.